

A front-tracking method for computation of interfacial flows with soluble surfactants

Metin Muradoglu^{a,*}, Gretar Tryggvason^{b,1}

^a *Department of Mechanical Engineering, Koc University, Rumelifeneri Yolu, Sariyer 34450 Istanbul, Turkey*

^b *Department of Mechanical Engineering, Worcester Polytechnic Institute, 100 Institute Road, Worcester, MA 01609-2280, United States*

Received 26 June 2007; received in revised form 5 September 2007; accepted 1 October 2007
Available online 12 October 2007

Abstract

A finite-difference/front-tracking method is developed for computations of interfacial flows with soluble surfactants. The method is designed to solve the evolution equations of the interfacial and bulk surfactant concentrations together with the incompressible Navier–Stokes equations using a non-linear equation of state that relates interfacial surface tension to surfactant concentration at the interface. The method is validated for simple test cases and the computational results are found to be in a good agreement with the analytical solutions. The method is then applied to study the cleavage of drop by surfactant—a problem proposed as a model for cytokinesis [H.P. Greenspan, On the dynamics of cell cleavage, *J. Theor. Biol.* 65(1) (1977) 79; H.P. Greenspan, On fluid-mechanical simulations of cell division and movement, *J. Theor. Biol.*, 70(1) (1978) 125]. Finally the method is used to model the effects of soluble surfactants on the motion of buoyancy-driven bubbles in a circular tube and the results are found to be in a good agreement with available experimental data.
© 2007 Elsevier Inc. All rights reserved.

Keywords: Soluble surfactant; Front-tracking method; Drop cleavage; Buoyancy-driven flow

1. Introduction

The surface active agents (surfactants) that are present as impurities or are added deliberately to the bulk fluid can critically affect the dynamics of multiphase flow systems [24]. Surfactants may also be created at the interface as a result of chemical reaction between the drop fluid and solutes in the bulk fluid [10,30]. Surfactant molecules typically consist of a hydrophilic head and a hydrophobic tail—detergents are common examples. They are collected at the fluid interfaces forming a buffer zone between the continuous fluid and the drop fluid molecules, and thus decrease the interfacial tension [20,24]. Surfactants are widely used in numerous important

* Corresponding author. Tel.: +90 212 338 14 73; fax: +90 212 338 15 48.

E-mail addresses: mmuradoglu@ku.edu.tr (M. Muradoglu), gretar@wpi.edu (G. Tryggvason).

¹ Tel.: +1 508 31 52 22; fax: +1 508 831 57 74.

scientific and engineering applications. In particular, surfactants can be used to manipulate drops and bubbles in microchannels [10,23], and to synthesize micron or submicron size monodispersed drops and bubbles for microfluidic applications [2].

The interfacial surface tension is generally a function of the surfactant concentration according to an equation of state. Non-uniform surfactant concentration leads to non-uniform normal (capillary) and tangential (Marangoni) stresses which can significantly affect the motion and deformation of drops and bubbles. Surfactants are sometimes added to the bulk or drop fluid to manipulate the interfacial flows [23]. In addition, surfactant plays a vital role to reduce the work required to expand lungs with each breath by reducing the surface tension of the liquid lining alveoli and airways. A lack of pulmonary surfactant production in premature neonates causes respiratory distress syndrome (RDS) [3]. In some cases, however, their presence is not desired but it is difficult to remove them from the system.

Computational modeling of interfacial flows with soluble surfactants is a challenging task. Surfactants are advected and diffused both at the interface and in the bulk fluid by the motion of fluid and by molecular mechanism, respectively. Therefore the evolution equations of the surfactant concentrations at the interface and in the bulk fluid must be solved coupled with the flow equations. The surfactant concentration at the interface alters the interfacial tension and thus alters the flow field in a complicated way. This interaction between the surfactant and the flow field is highly non-linear and poses a computational challenge.

Most previous computational studies of the effects of surfactants pertain to extensional flows in the context of Stokes flow. Stone and Leal [26] investigated the effects of insoluble surfactants on the deformation and breakup of drops. They determined that the degree of deformation is influenced by the accumulation of surfactant at the ends of the drop caused by the external flow, i.e., axial extension in their case. Milleken et al. [21] generalized their work for a range of drop fluid viscosities and a non-linear equation of state for the interfacial tension. They found that surfactants facilitate the formation of pointed ends during drop stretching and suggested that this was the reason for tip-streaming observed in experiments. More recently, Eggleton et al. [9] used a boundary integral method to investigate the onset of tip-streaming again in a linear extensional flow. They found that, similar to Stone and Leal [26], surfactant accumulates at the drop poles where it drives the surface tension to near zero. They also observed that the drop assumes a transient shape with highly pointed tips from which thin liquid threads are pulled. When the initial surfactant coverage is sufficiently high, this may lead to breakup in a tail-streaming mode. He et al. [15] studied the effects of surfactants on the motion of viscous drops in a capillary tube in the low Reynolds number limit and demonstrated the retarding effect of surfactant. Borhan and Mao [4] computationally studied the effects of surfactants and drop deformation using a boundary element method. They found that the accumulation of surfactant near the trailing edge of the drop may induce a re-entrant cavity at the back of the drop. Similar behavior has also been observed by Tsai and Miksis [28]. Johnson and Borhan [18] have studied the effects of surfactant solubility in cylindrical capillaries in the Stokes flow regime using a boundary integral method. There have been a handful of computational studies on the effect of surfactants on drop motion using full Navier–Stokes models. Drumright-Clarke and Renardy [7] studied the effects of insoluble surfactant on the motion and breakup of viscous drops in shear flows using a volume-of-fluid (VOF) method. Fujioka and Grotberg [11] used a finite-volume method to study the steady propagation of surfactant-laden plug in a two-dimensional channel. Lee and Pozrikidis [19] studied the effects of insoluble surfactants on the deformation of drops and bubbles in two-dimensional channels. James and Lowengrub [16] developed a surfactant-conserving volume-of-fluid method to study the effects of insoluble surfactants on interfacial flows. Xu et al. [31] presented a level-set method for computations of interfacial flows with insoluble surfactants and applied it to study effects of insoluble surfactants on single drops, drop–drop interactions and interactions of many drops. Recently Zhang et al. [33] developed a front-tracking method for simulations of a deformable bubble moving in a tube in the presence of a soluble or insoluble surfactant.

This paper presents a general computational framework based on the front-tracking method [27] for simulations of interfacial flows with soluble surfactants. In this method, both the bulk and interface surfactant concentration equations are solved coupled with the incompressible flow equations. In particular, the bulk surfactant concentration is allowed to vary both in space and time according to a convection–diffusion equation. The surfactant transfer between the bulk fluid and the interface is modeled in a conservative manner by distributing the amount of surfactant adsorbed by the interface as a negative source term for the bulk concen-

tration equation near the interface using a distribution scheme widely used in front-tracking methods [27]. Note that the present method fundamentally differs from that of Zhang et al. [33] in treating the mass transfer between the bulk fluid and drop interface. In the method proposed by Zhang et al. [33], the mass flux is approximated at the interface, i.e., the surfactant adsorption or desorption takes place exactly at the interface while, in the present method, the surfactant is adsorbed or desorbed in a thin *adsorption* layer adjacent to the interface. The present treatment is more consistent with the basic idea of the immersed boundary method used in the front-tracking algorithm. In addition, it also removes the potential numerical stiffness associated with sharp surfactant concentration gradient in the bulk fluid near the interface. The method has been validated for a number of test cases for which analytical solutions are available. The method is then applied to study the drop cleavage by surfactant—a problem that was proposed as a model for biological cell cytokinesis by Greenspan [12,13] and was more recently studied by He and Dembo [14]. Finally, the method is used to simulate the effects of a surfactant on the motion and deformation of a buoyancy-driven bubble rising in an axisymmetrical tube. It is first shown that a contaminated bubble behaves like a solid sphere rather than a fluid sphere in the limit of low Reynolds number and the terminal velocity of the contaminated bubble approaches that of a solid sphere as observed experimentally in numerous previous studies collected by Clift et al. [6]. The effects of the channel size on the terminal velocity of the bubble are also studied both for the clean and contaminated bubbles and the computational results are found to be in a good agreement with the available experimental data [6]. The grid convergence and mass conservation of surfactant in the bulk and at the interface are demonstrated.

In the next section, the governing equations for multiphase/multifluid flows with surfactants are described and the numerical algorithm is presented in Section 3. The accuracy of the numerical algorithm is demonstrated in Section 4 using simple test cases for which analytical solutions are available. Some computational examples are presented and discussed in Section 5 and finally conclusions are drawn in Section 6.

2. Mathematical formulation

Consider the axisymmetrical motion and deformation of a viscous drop moving in a circular tube as sketched in Fig. 1. The flow equations are described here in the context of the finite-difference/front-tracking

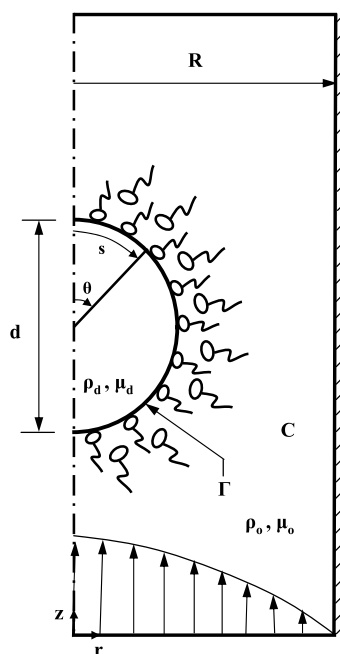


Fig. 1. Schematic illustration of the axisymmetric motion and deformation of a contaminated bubble moving in a circular tube.

(FD/FT) method. The fluid motion is assumed to be governed by the incompressible Navier–Stokes equations and we solve for the flow everywhere, both inside and outside of the drop. Following Unverdi and Tryggvason [29], a single set of governing equations can be written for the whole computational domain as long as the jump in material properties such as density, viscosity and molecular diffusion coefficient is correctly accounted for and surface tension is included.

The Navier–Stokes equations in conservative form are given by

$$\frac{\partial \rho \mathbf{u}}{\partial t} + \nabla \cdot (\rho \mathbf{u} \mathbf{u}) = -\nabla p + \nabla \cdot \mu (\nabla \mathbf{u} + \nabla \mathbf{u}^T) + \int_A \sigma(\Gamma) \kappa \mathbf{n} \delta(\mathbf{x} - \mathbf{x}_f) dA, \tag{1}$$

where \mathbf{u} is the velocity, p is the pressure, and ρ and μ are the discontinuous density and viscosity fields, respectively. The effects of surface tension is included as a body force in the last term on the right hand side, where σ is the surface tension that is function of the surfactant concentration Γ at the interface, κ is twice the mean curvature, and \mathbf{n} is a unit vector normal to the interface. The surface tension acts only on the interface as indicated by the three-dimensional delta function δ whose arguments \mathbf{x} and \mathbf{x}_f are the point at which the equation is evaluated and a point at the interface, respectively.

The Navier–Stokes equations are supplemented by the incompressibility condition:

$$\nabla \cdot \mathbf{u} = 0. \tag{2}$$

We also assume that the material properties remain constant following a fluid particle, i.e.,

$$\frac{D\rho}{Dt} = 0; \quad \frac{D\mu}{Dt} = 0, \tag{3}$$

where D/Dt is the material derivative. The density and viscosity vary discontinuously across the fluid interface and are given by

$$\begin{aligned} \rho &= \rho_d I(r, z, t) + \rho_o (1 - I(r, z, t)), \\ \mu &= \mu_d I(r, z, t) + \mu_o (1 - I(r, z, t)), \end{aligned} \tag{4}$$

where the subscripts “ d ” and “ o ” denote the properties of the drop and bulk fluid, respectively, and $I(r, z, t)$ is the indicator function defined as

$$I(r, z, t) = \begin{cases} 1 & \text{in drop fluid,} \\ 0 & \text{in bulk fluid.} \end{cases} \tag{5}$$

Concentration of surfactant on the interface, Γ , is defined as

$$\Gamma = \frac{M_s}{A}, \tag{6}$$

where M_s is the total mass of surfactant and A is the surface area. The surface tension decreases proportional to the surfactant concentration at the interface according to the equation of state derived from Langmuir adsorption [20]

$$\sigma = \sigma_s + \mathcal{R} T \Gamma_\infty \ln \left(1 - \frac{\Gamma}{\Gamma_\infty} \right), \tag{7}$$

where \mathcal{R} is the ideal gas constant, T is the absolute temperature, σ_s is the surface tension of clean interface and Γ_∞ is the maximum packing concentration. Eq. (7) can also be written as

$$\sigma = \sigma_s \left[1 + \beta_s \ln \left(1 - \frac{\Gamma}{\Gamma_\infty} \right) \right], \tag{8}$$

where $\beta_s = \frac{\mathcal{R} T \Gamma_\infty}{\sigma_s}$ is the elasticity number. Eq. (8) provides a good model for low interfacial surfactant concentrations but it deviates significantly as the surfactant concentration increases and results in unphysical negative surface tension in the high surfactant concentration limit. Since the present study emphasizes on the numerical method rather than the physical models, Eq. (8) is slightly modified to avoid negative values of the surface tension as

$$\sigma = \sigma_s \left[\max \left(\epsilon_\sigma, 1 + \beta_s \ln \left(1 - \frac{\Gamma}{\Gamma_\infty} \right) \right) \right], \quad (9)$$

where ϵ_σ is taken as 0.05 in the present study. The surfactant concentration Γ evolves by [25]

$$\frac{\partial \Gamma}{\partial t} + \nabla_s \cdot (\Gamma \mathbf{U}_s) = D_s \nabla_s^2 \Gamma + \dot{S}_\Gamma, \quad (10)$$

where the gradient operator along the interface is defined as

$$\nabla_s = \nabla - \mathbf{n}(\mathbf{n} \cdot \nabla). \quad (11)$$

In Eq. (10), \mathbf{U}_s is the tangential velocity on the interface, D_s is the diffusion coefficient along the interface and \dot{S}_Γ is the source term given by

$$\dot{S}_\Gamma = k_a C_s (\Gamma_\infty - \Gamma) - k_b \Gamma, \quad (12)$$

where k_a and k_b are adsorption and desorption coefficients, respectively, and C_s is the concentration of surfactant in fluid immediately adjacent to the interface. The bulk surfactant concentration C is governed by the advection–diffusion equation in the form

$$\frac{\partial C}{\partial t} + \nabla \cdot (C \mathbf{u}) = \nabla \cdot (D_{co} \nabla C), \quad (13)$$

where the coefficient D_{co} is related to the molecular diffusion coefficient D_c and the indicator function I as

$$D_{co} = D_c (1 - I(r, z, t)). \quad (14)$$

The source term is related to the bulk concentration by [8],

$$\dot{S}_\Gamma = -D_{co} (\mathbf{n} \cdot \nabla C|_{\text{interface}}). \quad (15)$$

In the present method, the boundary condition at the interface given by Eq. (15) is first converted into a source term in a conservative manner following the same philosophy as for the immersed boundary method [22]. We assume that all the mass transfer between the interface and bulk takes place in a thin *adsorption* layer adjacent to the interface as sketched in Fig. 2(a) so that the total amount of mass adsorbed on the interface is distributed over the adsorption layer and added to the bulk concentration evolution equation as a negative source term in a conservative manner. Eq. (13) thus becomes

$$\frac{\partial C}{\partial t} + \nabla \cdot (C \mathbf{u}) = \nabla \cdot (D_{co} \nabla C) + \dot{S}_C, \quad (16)$$

where \dot{S}_C is the source term evaluated at the interface and distributed onto the adsorption layer in a conservative manner as discussed in Section 3.3. With this formulation, all the mass of the bulk surfactant to be adsorbed by the interface has been already consumed in the adsorption layer before the interface so the boundary condition at the interface simplifies to be $\mathbf{n} \cdot \nabla C|_{\text{interface}} = 0$.

The governing equations are solved in their dimensional forms but the results are expressed in terms of relevant non-dimensional quantities. Let \mathcal{L} and \mathcal{U} be appropriately defined length and velocity scales, respectively, and $\mathcal{T} = \mathcal{L}/\mathcal{U}$ be the time scale, then governing non-dimensional numbers can be summarized as

$$\begin{aligned} Re &= \frac{\rho_o \mathcal{U} \mathcal{L}}{\mu_o}; & Ca &= \frac{\mu_o \mathcal{U}}{\sigma_s}; & Pe_c &= \frac{\mathcal{U} \mathcal{L}}{D_c}; & Pe_s &= \frac{\mathcal{U} \mathcal{L}}{D_s}; & \frac{\rho_d}{\rho_o}; & \frac{\mu_d}{\mu_o}; \\ k &= \frac{k_a C_\infty}{k_b}; & Bi &= \frac{k_b \mathcal{L}}{\mathcal{U}}; & Da &= \frac{\Gamma_\infty}{\mathcal{L} C_\infty}; & \beta_s &= \frac{\mathcal{R} T \Gamma_\infty}{\sigma_s}, \end{aligned} \quad (17)$$

where Re , Ca , Pe_c , Pe_s , k , Bi , Da and β_s are the Reynolds number, the capillary number, the Peclet number based on bulk surfactant diffusivity, the Peclet number based on interface surfactant diffusivity, the dimensionless adsorption depth, Biot number, Damkohler number and the elasticity number, respectively.

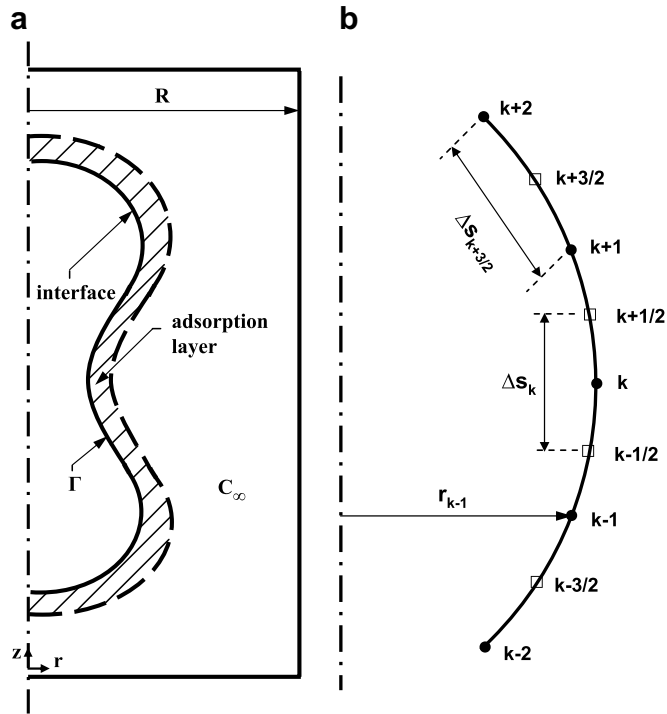


Fig. 2. (a) Schematic illustration of the adsorption layer. (b) Sketch for the spatial discretization of the surfactant concentration evolution equation on the interface. The open symbols represent the location of Lagrangian marker points while the filled symbols represent the front element centroids.

3. Numerical solution procedure

The flow equations are solved together with the bulk and interface surfactant concentration evolution equations using a FD/FT method [27,29]. In this method, the interface is represented by connected Lagrangian marker points moving with the local flow velocity interpolated from the neighboring stationary regular Cartesian Eulerian grid as sketched in Fig. 3. A piece of the interface between two neighboring marker points is

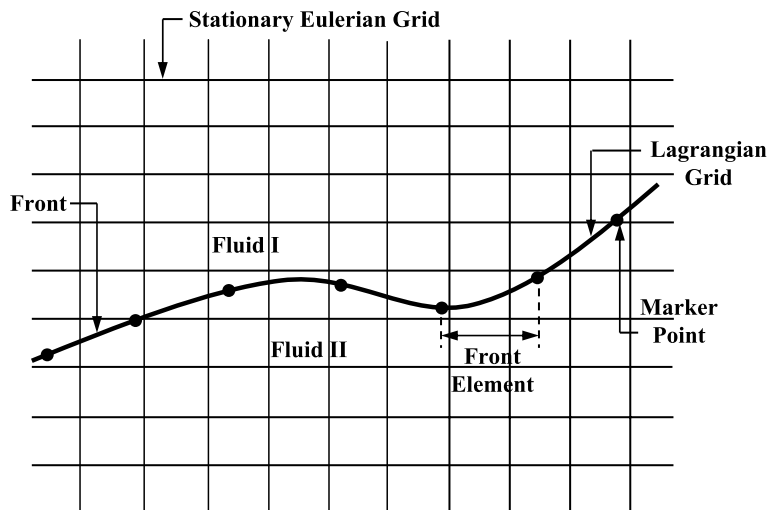


Fig. 3. Schematic illustration of the computational grids employed.

called a front element. The material properties inside and outside of the drop are set based on the indicator function defined by Eq. (5). The indicator function is computed on the Eulerian grid using the same procedure as described by Tryggvason et al. [27]. The method is briefly outlined here. The discontinuity is spread onto the grid points adjacent to the interface resulting in the gradient field

$$\mathbf{G}(\mathbf{x}) = \nabla I = \int_A \mathbf{n} \delta(\mathbf{x} - \mathbf{x}_f) dA, \tag{18}$$

which is zero everywhere except at the interface. Note that the vector field \mathbf{G} is also utilized to enforce the no mass flux boundary condition for the bulk surfactant concentration at the interface as will be discussed in Section 3.3. Taking the divergence of both sides of Eq. (18) yields

$$\nabla^2 I = \nabla \cdot \mathbf{G}, \tag{19}$$

which is a separable Poisson equation and can be solved efficiently in the vicinity of the drop. The delta function appearing in Eq. (18) is approximated by Peskin’s cosine distribution function [22]. The same function is also used to distribute the surface tension forces computed at the center of front elements over the neighboring grid points and also to interpolate the velocity vector from the Eulerian grid onto the marker points. This distribution function is sketched in Fig. 4(a). In Eq. (19), the divergence operator is approximated using second order central differences and then the Poisson equation is solved using a fast Poisson solver [1]. The computed indicator function is constant in each material region but with a finite-thickness transition zone at the interface. Therefore the transition region approximates a two-dimensional Heaviside function.

The Lagrangian grid is also used to compute the surface tension forces at the interface which are then distributed over the neighboring Eulerian grid cells as body forces in a conservative manner [27,29] using Peskin’s distribution function. Since the FD/FT method has been described in details by Unverdi and Tryggvason [29] and by Tryggvason et al. [27] for surfactant-free flows, the basic flow solver is discussed only briefly here for completeness and emphasis is placed on the solution of the bulk and interfacial surfactant concentration evolution equations.

3.1. Flow solver

The flow equations (Eqs. (1) and (2)) are solved on a stationary staggered Eulerian grid. The spatial derivatives are approximated using second order central finite-differences for all field quantities. The time integration is achieved using a projection method originally developed by Chorin [5]. Following Unverdi and Tryggvason [29], Eqs. (1) and (2) are written in the form

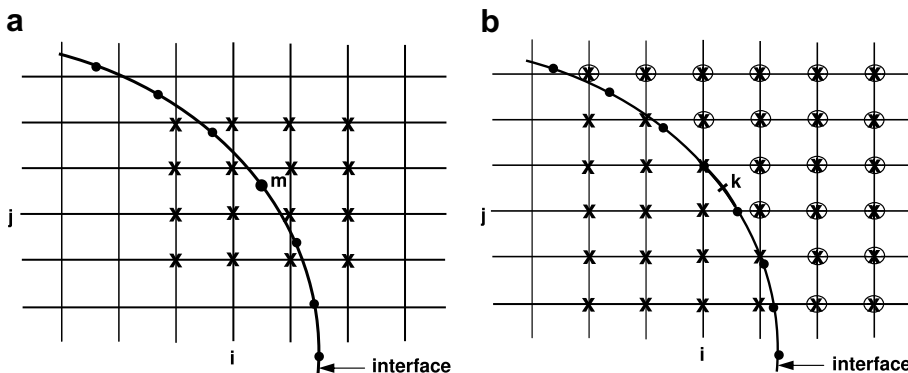


Fig. 4. Sketch for interpolation schemes. (a) Velocity is interpolated onto the location of m th marker point from 16 neighboring Eulerian grid nodes. Similarly, the surface tension force computed at the front element centroid is distributed onto 16 neighboring Eulerian grid nodes. (b) The bulk surfactant concentration is interpolated from the Eulerian grid nodes outside of the drop onto k th front element and the source term computed on the front element is distributed onto the same Eulerian grid nodes.

$$\frac{\rho^{n+1}\mathbf{u}^{n+1} - \rho^n\mathbf{u}^n}{\Delta t} = \mathbf{A}^n - \nabla p, \tag{20}$$

$$\nabla \cdot \mathbf{u}^{n+1} = 0, \tag{21}$$

where \mathbf{A} is the advective, diffusive and body force terms in Eq. (1). Then the above equation is decomposed as

$$\frac{\rho^{n+1}\mathbf{u}^* - \rho^n\mathbf{u}^n}{\Delta t} = \mathbf{A}^n, \tag{22}$$

$$\frac{\rho^{n+1}\mathbf{u}^{n+1} - \rho^{n+1}\mathbf{u}^*}{\Delta t} = -\nabla p, \tag{23}$$

where \mathbf{u}^* is a provisional velocity ignoring the effect of the pressure. Next the unprojected velocity field is computed from Eq. (22) and then the pressure field is computed as follows: taking the divergence of Eq. (23) and using the incompressibility condition given by Eq. (21), we obtain a non-separable Poisson equation for pressure in the form

$$\nabla \cdot \frac{1}{\rho^{n+1}} \nabla p = -\frac{1}{\Delta t} \nabla \cdot \mathbf{u}^*, \tag{24}$$

which is solved on the Eulerian grid using a multigrid method as described by Tryggvason et al. [27]. Finally the velocity field at the new time level is computed as

$$\mathbf{u}^{n+1} = \mathbf{u}^* - \frac{\Delta t}{\rho^{n+1}} \nabla p. \tag{25}$$

In the present paper we use a first order explicit time integration method for the time derivatives as described above. However, second order time integration can be easily achieved by a predictor corrector method as discussed by Tryggvason et al. [27].

3.2. Surfactant concentration at interface

The evolution equation of the surfactant concentration at the interface is solved on the Lagrangian grid. From Eqs. (10) and (11), we obtain

$$\frac{\partial \Gamma}{\partial t} + \nabla \cdot (\Gamma \mathbf{U}_s) - \Gamma \mathbf{n} \cdot \nabla \mathbf{U}_s \cdot \mathbf{n} = D_s \nabla_s^2 \Gamma + \dot{S}_\Gamma. \tag{26}$$

On the other hand, the area of an element of the interface evolves by [16]

$$\frac{DA}{Dt} = \frac{\partial A}{\partial t} + \mathbf{U}_s \cdot \nabla A = -A(\mathbf{n} \cdot \nabla \mathbf{u} \cdot \mathbf{n}). \tag{27}$$

Combining Eqs. (26) and (27), one obtains

$$\frac{d\Gamma A}{dt} = AD_s \nabla_s^2 \Gamma + A\dot{S}_\Gamma. \tag{28}$$

For an axisymmetric problem, Eq. (28) can be written as

$$\frac{d\Gamma A}{dt} = A \left(D_s \frac{1}{r} \frac{\partial}{\partial s} \left(r \frac{\partial \Gamma}{\partial s} \right) + \dot{S}_\Gamma \right), \tag{29}$$

where s is the arc length along the interface and r is the radial coordinate in cylindrical coordinates. Eq. (29) can be expressed in compact form as

$$\frac{d\Gamma A}{dt} = Af(\Gamma, t), \tag{30}$$

where f is given by

$$f(\Gamma, t) = D_s \frac{1}{r} \frac{\partial}{\partial s} \left(r \frac{\partial \Gamma}{\partial s} \right) + \dot{S}_\Gamma. \tag{31}$$

Referring to the sketch in Fig. 2(b), the right hand side of Eq. (29) is discretized using central differences as,

$$[Af]_k \equiv \frac{A_k}{r_k} D_s \left[\frac{r_{k+\frac{1}{2}} \frac{\Gamma_{k+1} - \Gamma_k}{s_{k+1} - s_k} - r_{k-\frac{1}{2}} \frac{\Gamma_k - \Gamma_{k-1}}{s_k - s_{k-1}}}{s_{k+\frac{1}{2}} - s_{k-\frac{1}{2}}} \right] + A_k \dot{S}_{\Gamma_k}, \quad (32)$$

where k denotes the k th front element whose surface area is approximated as $A_k \equiv \frac{1}{2}(r_{k+\frac{1}{2}} + r_{k-\frac{1}{2}})\Delta s_k$. The time-integration is performed using a simple explicit Euler method, i.e.,

$$\Gamma^{n+1} = \frac{1}{A^{n+1}} [\Gamma^n A^n + \Delta t A^n f(\Gamma^n, t_n)]. \quad (33)$$

3.3. Bulk surfactant concentration

The bulk surfactant concentration equation is solved on the staggered Eulerian grid. The bulk surfactant concentration is located at the pressure nodes. The spatial derivatives are approximated using second order central differences and time integration is performed using a first order explicit Euler method. The source term is first computed on the interface and is then distributed over the adsorption layer in a conservative manner. For this purpose, the distribution algorithm is slightly modified as follows: The source term $\dot{S}_{C_{i,j}}$ at grid point (i, j) is approximated as

$$\dot{S}_{C_{i,j}} = - \sum_k \omega_{i,j}^k \dot{S}_{\Gamma_k} \frac{r_k \Delta l_k}{r_{i,j} h^2}, \quad (34)$$

where \dot{S}_{Γ_k} is the source term evaluated at the center of the k th element, r_k and Δl_k are the radial coordinate of the center and the arc length of the k th element, $r_{i,j}$ is the radial coordinate of the grid node (i, j) , h is the grid spacing and $\omega_{i,j}^k$ is the weight of grid point (i, j) , respectively. The weight must satisfy the consistency condition

$$\sum_i \sum_j \omega_{i,j}^k = 1 \quad (35)$$

in order to conserve the total source strength in going from the interface to the grid. The weight for the grid point (i, j) , for smoothing from the center of the k th element (r_f^k, z_f^k) , can be written as

$$\omega_{i,j}^k = \frac{\tilde{\omega}_{i,j}^k}{\sum_i \sum_j \tilde{\omega}_{i,j}^k}, \quad (36)$$

where the non-normalized weight function is defined as

$$\tilde{\omega}_{i,j}^k = d_c(r_f^k - ih) d_c(z_f^k - jh). \quad (37)$$

In Eq. (37), the distribution function d_c is a slightly modified version of the Peskin's cosine distribution defined as

$$d_c(x) = \begin{cases} \frac{1}{2W} (1 + \cos(\frac{\pi x}{W})) & \text{if } |x| < W \text{ and } I < 0.5, \\ 0, & \text{otherwise,} \end{cases} \quad (38)$$

where W is the width of the “adsorption” layer, taken as $W = 2h$ in the present study. Note that we have also tested a wider layer, i.e., $W = 3h$ and found that the results are not very sensitive to the width. As can be seen in Eq. (38), the source term is distributed only outside of the drop region, i.e., $I(r, z, t) \leq 0.5$, which is illustrated schematically in Fig. 4(b).

As mentioned before, in the present method, the mass exchange between the bulk fluid and the interface occurs in an “adsorption” layer (see Fig. 2(a)) so that the proper boundary condition for the bulk concentration at the interface becomes $\mathbf{n} \cdot \nabla C_{\text{interface}} = 0$. This condition is imposed approximately as follows: Referring to the sketch in Fig. 5, the no mass flux across the interface is imposed approximately by setting the bulk concentration at grid points inside the drop, i.e., at point (i, j) in the figure, to the bulk concentration at the point of reflection with respect to the interface, i.e., at point “o” in the figure. The bulk concentration at the reflection point is approximated using a bilinear interpolation. In the implementation, this is done only for the grid

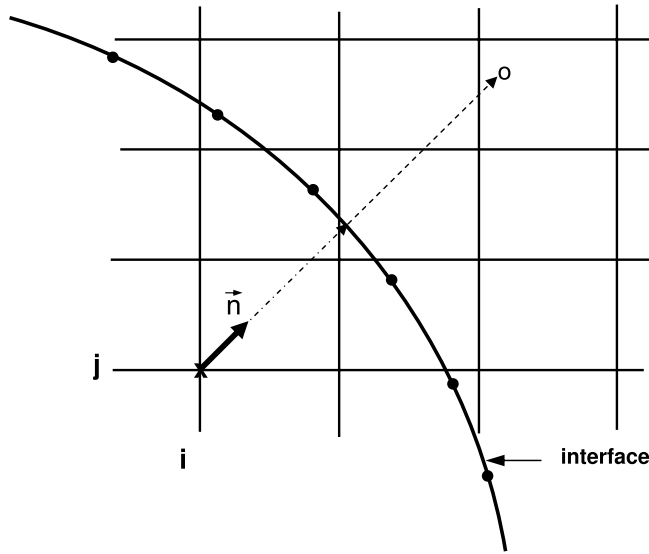


Fig. 5. Treatment of boundary condition for the bulk concentration at the interface.

points near the interface. For this purpose, the normal vectors that are already computed at the interface and distributed over the grid points in the vicinity of the interface during the process of computing the indicator function [27] are utilized. First the intersection point at the interface in the direction of the normal vector is computed and then the reflection point “o” is computed as shown in the figure. We found that this procedure is robust and computationally very efficient.

3.4. Overall solution procedure

The finite-difference and front-tracking methods are combined as follows. In advancing the solutions from time step n to step $n + 1$, first the unprojected velocity field is computed from Eq. (22) and then the marker points are moved for a single time step by

$$\mathbf{X}_p^{n+1} = \mathbf{X}_p^n + \Delta t \mathbf{V}_p^n, \tag{39}$$

where \mathbf{X}_p and \mathbf{V}_p are the positions of the front marker points and the velocity interpolated from the neighboring Eulerian grid nodes onto the front location \mathbf{X}_p using the Peskin’s distribution, respectively. Next the bulk and interface surfactant concentrations are advanced for a single time step as explained above. Then the material properties are evaluated based on the new locations of the marker points as

$$\rho^{n+1} = \rho(\mathbf{X}_p^{n+1}), \quad \mu^{n+1} = \mu(\mathbf{X}_p^{n+1}), \quad \sigma^{n+1} = \sigma(\Gamma^{n+1}). \tag{40}$$

Finally the projected velocity field is computed from Eq. (23). Note that the Lagrangian grid is restructured at every time step by deleting front elements that are smaller than a prespecified lower limit and splitting front elements that are larger than a prespecified upper limit in the same way as described by Tryggvason et al. [27] in order to keep the front element sizes nearly uniform and comparable to the Eulerian grid size. Restructuring the Lagrangian grid is of crucial importance since it avoids unresolved wiggles due to small elements and lack of resolution due to large elements. The restructuring of the Lagrangian grid is performed such that the mass conservation is strictly satisfied for the surfactant at the interface as follows. The total mass of surfactant on the parent element is computed before splitting and is then distributed onto the newly created daughter elements in proportion to their surface areas in a conservative manner. Similarly, the amount of surfactant mass on the small element that is to be deleted is distributed onto its immediate neighboring elements again in proportion to their surface areas in a conservative manner. Note that the surface areas of the neighboring front elements are computed after the deletion.

The time step is restricted to maintain numerical stability. In the present study, the restrictions due to diffusion, convection and surface tension are considered. The time step is given by

$$\Delta t = \min \left(\frac{h_{\min}^2}{4s_{\max}}, \frac{2s_{\min}}{U_{\max}^2}, \sqrt{\frac{(\rho_o + \rho_d)h_{\min}^3}{4\pi\sigma}} \right), \quad (41)$$

where s_{\min} and s_{\max} are the largest and the smallest values, respectively, among the kinematic viscosity $\nu = \mu/\rho$ and molecular diffusion coefficient D_c , h_{\min} is the smallest grid size and U_{\max} is the maximum magnitude of the velocity in the domain. Note that the time step given by Eq. (41) is multiplied by a safety factor typically taken as 0.85 in the present study in order to avoid instabilities due to non-linear effects.

4. Validation

A number of test cases were performed to validate the numerical solution algorithm. Since the FD/FT method is not new and it has been validated for surfactant-free cases many times before as reviewed by Tryggvason et al. [27], tests are performed to validate it for the surfactant cases. For this purpose, simple test cases are designed to validate the numerical approximations to each term in Eqs. (16) and (28), and the results are compared with analytical solutions.

4.1. Convection test

A simple test is performed to validate the numerical approximations to the convective terms in the surfactant evolution equation. Consider a sphere that continuously expands in the normal direction with a constant radial velocity as sketched in Fig. 6(a). The initial surfactant concentration is uniform on the sphere. Both the diffusion and the source terms are switched off so that the surfactant concentration changes solely due to the change in the surface area of the drop. For this case, Eq. (28) simply becomes

$$\frac{d\Gamma A}{dt} = 0, \quad (42)$$

which can be integrated to get

$$\Gamma^*(t) = \frac{A_0}{A(t)} \Gamma_0^*, \quad (43)$$

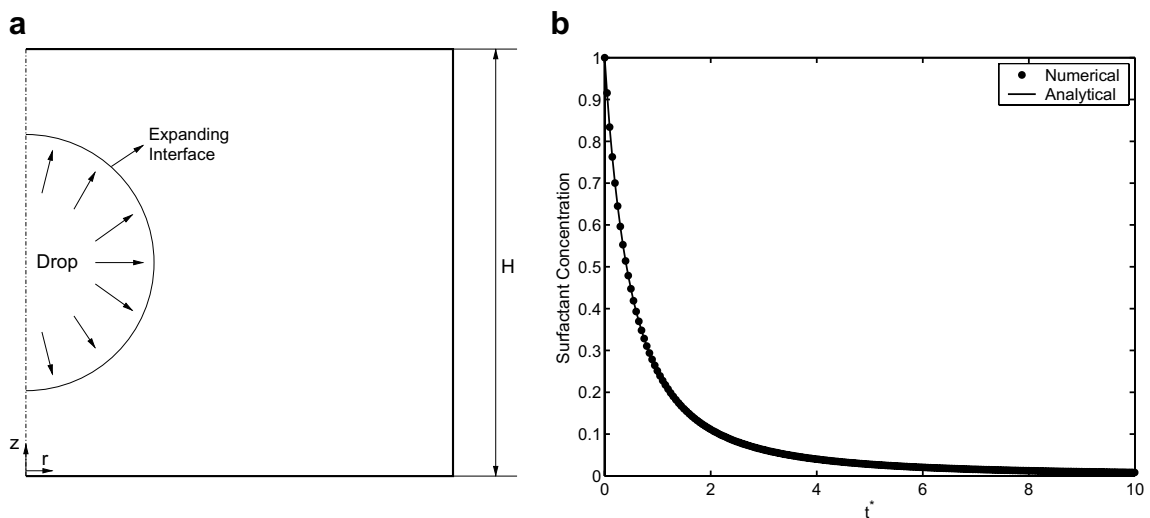


Fig. 6. Convection test. (a) Schematic representation of the expanding spherical interface. (b) Evolution of surfactant concentration in time for a continuously expanding spherical interface when both the diffusion and source terms are switched off.

where $\Gamma^* = \Gamma/\Gamma_\infty$. In Eq. (43), A_0 and Γ_0^* are the initial surface area and the initial surfactant concentration, respectively. The numerical and analytical solutions for the variation of surfactant concentration in time are plotted in Fig. 6(b). The numerical results are obviously in an excellent agreement with the analytical solution, indicating accurate discretization of the convective terms.

4.2. Interface diffusion test

In order to test the diffusive terms in the surfactant concentration at the interface, a spherical interface of radius a is kept stationary and the source term \dot{S}_r is switched off. The initial surfactant concentration distribution is set to $\Gamma = \frac{1}{2}(1 - \cos \theta)$ where θ is the angle measured in clockwise direction as sketched in Fig. 1. The analytical solution for this problem is given by

$$\Gamma(\theta, t) = \frac{1}{2} \left(1 - e^{-\frac{2t^*}{Pe_s}} \cos \theta \right), \tag{44}$$

where $Pe_s = \mathcal{U}a/D_s$, $t^* = t\mathcal{U}/a$ and \mathcal{U} is an appropriately defined velocity scale.

The numerical results are compared with the analytical solution in Fig. 7(a) for $Pe_s = 10$ at various non-dimensional times, and in Fig. 7(b) for various Peclet numbers at time $t^* = 35$. As can be seen in these figures, the numerical results match very well with the analytical solution, indicating the accurate discretization of the diffusive terms.

4.3. Bulk concentration diffusion and mass transfer test

The next test case deals with the diffusion of the bulk concentration and the mass transfer between the bulk and the interface. Consider a stationary spherical drop of radius a suspended in a large channel. The drop interface is initially clean and the initial bulk surfactant concentration is uniform at $C = C_\infty$. The mass transfer is solely due to molecular diffusion. We also consider a simplified version of the source term as $\dot{S}_r = k_a C_s$ so that the mass transfer is always from the bulk fluid to the interface. For this simplified problem, the surfactant concentration in the bulk fluid evolves by

$$\frac{\partial C}{\partial t} = \frac{D_s}{r^2} \frac{\partial}{\partial r} \left(r^2 \frac{\partial C}{\partial r} \right), \tag{45}$$

which, for short times or in an infinite domain, can be solved to yield

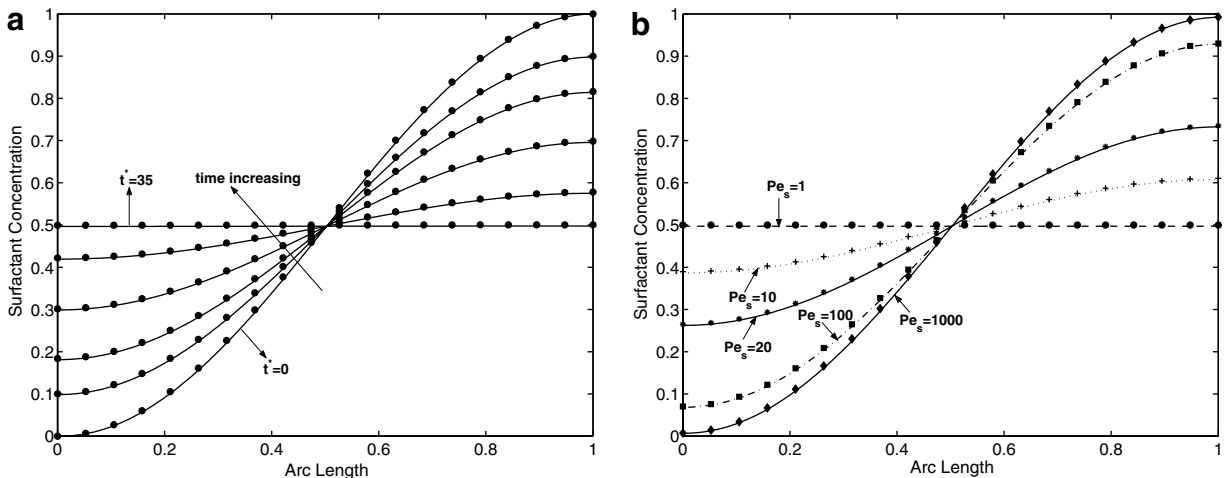


Fig. 7. Diffusion test for the surfactant concentration at the interface. (a) Time evolution of Γ for $Pe_s = 10$. (b) Surfactant concentration as a function of normalized arc length for various Peclet numbers at $t^* = 35$.

$$\frac{C_\infty - C}{C_\infty} = \frac{k_a \sqrt{\pi D_s t} / D_s}{1 + \frac{\sqrt{\pi D_s t}}{a} \left(1 + \frac{k_a a}{D_s}\right)} \frac{a}{r} \operatorname{erfc}\left(\frac{r-a}{2\sqrt{D_s t}}\right), \quad (46)$$

where $\operatorname{erfc}(x)$ is the complementary error function. The surfactant concentration at the interface is then given by

$$\frac{d\Gamma}{dt} = k_a C_s|_{r=a}, \quad (47)$$

which, using Eq. (46), can be integrated to yield

$$\Gamma = \Gamma_0 + k_a C_\infty \left(t - \frac{\omega h}{\eta^3} (\eta^2 t - 2\eta\sqrt{t} + 2\ln(1 + \eta\sqrt{t})) \right), \quad (48)$$

where Γ_0 is the initial surfactant concentration (set to zero here), $\omega = k_a/D_s$, $h = \sqrt{\pi D_s}$ and $\eta = \frac{h}{a}(1 + \omega a)$. Here the drop is placed at the center of a cylindrical tube that extends four drop radii in the radial direction and eight drop radii in the axial direction. The computational domain is resolved by a uniform Cartesian grid containing 128×256 grid cells. All quantities are made dimensionless using the length scale $\mathcal{L} = a$ and the time scale $\mathcal{T} = a^2/D_c$. Contour plots of the bulk surfactant concentration at various times are shown in Fig. 8 to demonstrate the evolution of the bulk surfactant concentration in time. As can be seen, the bulk surfactant concentration contours remain spherically symmetric until the disturbances reach the outer wall, which qualitatively indicates the accuracy of the computational results. This is quantified in Fig. 9(a) and (b). The computed bulk surfactant concentration profiles taken along the horizontal plane passing through the center of the drop are compared with the analytical solution in Fig. 9 at various times. The computational profiles agree well with the analytical solution except at very early times where steep gradients near the interface lead to large numerical errors and after the disturbances reach the outer wall where the analytical solution is not valid. Finally, the surfactant concentration at the interface is plotted in Fig. 9(b) and is again compared with the analytical solution. The computations are performed using various grid resolutions ranging from 16×32 to 128×256 grid cells. The figure shows clearly that the computational results converge to the analytical solution as the computational grid is refined. The grid convergence of the method is also examined in details in Section 5.

4.4. Test for the Marangoni effects

The final test concerns the effects of the Marangoni stresses. For this purpose, we consider a test case that is equivalent to the thermocapillary migration of a viscous drop at vanishing Reynolds and Marangoni numbers

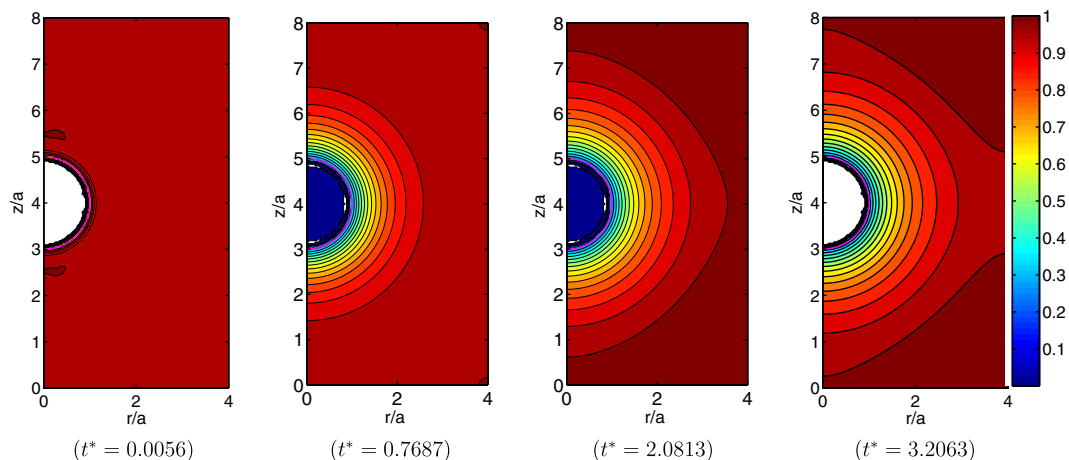


Fig. 8. Diffusion test for the bulk surfactant concentration. The contours of constant bulk surfactant concentration at various times. Grid: 128×256 . (For interpretation of the references to colours, the reader is referred to the web version of this paper.)

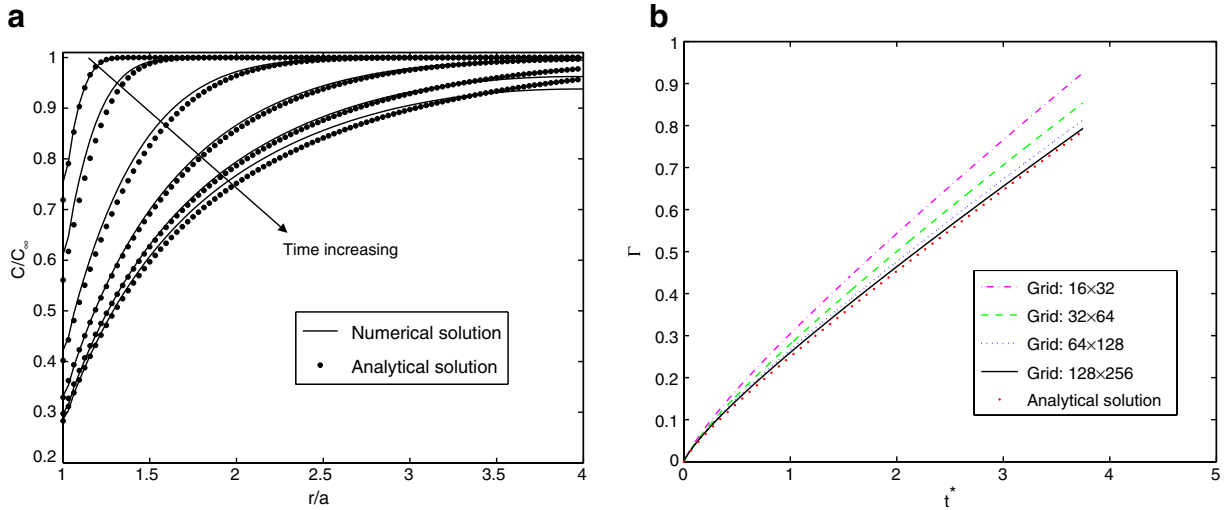


Fig. 9. Bulk surfactant concentration diffusion test. (a) Bulk surfactant concentration profiles at times $t^* = 0.0056, 0.030, 0.206, 0.787, 2.08$ and 3.21 . (b) The time evolution of the surfactant concentration at the interface computed using various grid resolutions.

studied theoretically by Young et al. [32]. In this test case, a viscous drop of radius a moves solely due to Marangoni stresses in an otherwise quiescent fluid in an axisymmetrical channel of radius $R = 5a$ and length $L = 15a$. The Marangoni stresses are caused by interfacial surfactant concentration specified as a function of the axial coordinate as

$$\frac{\Gamma}{\Gamma_\infty} = z/L, \tag{49}$$

and a linear equation of state is used in the form

$$\sigma = \sigma_s \left(1 - \beta_s \frac{\Gamma}{\Gamma_\infty} \right). \tag{50}$$

This test case corresponds to the thermocapillary migration of a viscous drop in a linear ambient temperature gradient and equal heat conductivities of the drop and the continuous fluids. For this case, the steady terminal velocity of the drop is given by [32]

$$V_{YGB} = \frac{2\sigma_s\beta_s a}{L(6\mu_o + 9\mu_d)}. \tag{51}$$

We put $\rho_o = \rho_d = 0.2$, $\mu_o = 0.1$, $\mu_d = 0.1$, $a = 0.5$ and $\beta_s = 2.0$ and compare the results with the theoretical result of Young et al. [32]. The computational domain is resolved by a 256×768 uniform grid. The pressure contours and velocity vectors in the vicinity of the drop are plotted in Fig. 10(a) after an approximate steady state has been achieved. The normalized terminal velocity is plotted in Fig. 10(b) as a function of non-dimensional time and is compared with the theoretical result. The plot shows that the drop velocity asymptotically approaches the theoretical results and at the end of the simulation the difference is below 3%. The Reynolds number, based on the final terminal velocity, is about $Re = 0.134$.

5. Computational examples

After validating the numerical solution algorithm for the test cases in the previous section, the method is first applied to study drop cleavage by a surfactant—a problem studied by Greenspan [12,13] as a model for cytokinesis. Then it is used to study the effects of surfactant on the buoyancy-driven motion and deformation of bubbles rising in a straight axisymmetrical tube of various diameters. For the second test the results are compared with available experimental data.

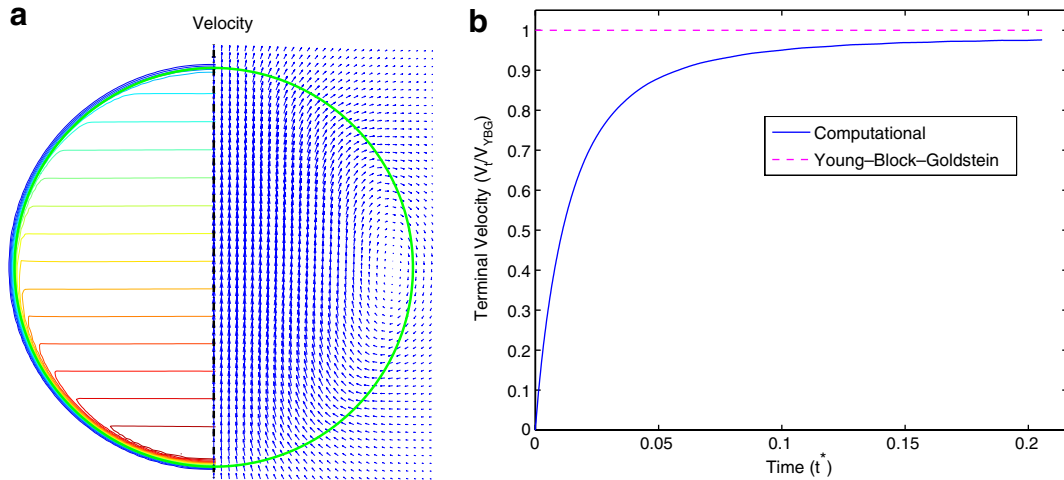


Fig. 10. Marangoni motion test. (a) The pressure contours (left side) and velocity vectors (right side) in the vicinity of the drop. (b) The terminal velocity versus time. The solid line denotes the computational result and dashed line is the theoretical result of Young et al. [32].

5.1. Cleavage of a viscous drop by surfactant

Greenspan [12,13] constructed a model for cleavage of biological cells in which the cell was simulated by a drop of oil suspended in a neutrally buoyant solvent and cleavage was mimicked by releasing controlled amount of surfactant at opposite poles of the droplet. His experiments showed that cleavage of a droplet is possible if the surfactant is sufficiently strong. The problem was also studied computationally more recently by He and Dembo [14]. This problem is studied here using the present FD/FT method. An initially clean droplet of radius a is placed at the center of a cylindrical tube that extends three drop radii in the radial direction and nine drop radii in the axial direction. Bulk surfactant is introduced instantaneously at the north and south poles of the droplet uniformly in a band extending $0.95a$ in the radial direction as shown in Fig. 11. To simulate the continuous surfactant supply from the poles as is done in the experiment, the surfactant concentration is kept constant in this band above the north pole and below the south pole. The results are presented in terms of non-dimensional quantities with $\mathcal{L} = a$, $\mathcal{T} = a\mu_o/\sigma_s$ and $\mathcal{U} = \sigma_s/\mu_o$ as length, time and velocity scales, respectively. The drop cleavage process is illustrated in Fig. 11 where the drop interface and contours of constant bulk surfactant concentration are plotted at various times. The computations are performed using a 128×384 uniform grid and the non-dimensional numbers are set to $Da = 0.0001$, $Bi = 15$, $k = 5$, $Pe_c = 500$, $Pe_s = 2000$ and $\beta_s = 0.95$. The density and viscosity ratios are set to unity and 2, respectively. The drop interface and the velocity field are plotted in Fig. 12 in the vicinity of the drop just before the breakup to illustrate the overall flow field. Note that the velocity vectors are shown at every third grid point in Fig. 12. The time evolution of the surfactant concentration at the interface is also shown in Fig. 13. The surfactant concentration increases at the interface near the north and south poles as time progresses and this reduces the surface tension at the poles and causes the drop to elongate in the axial direction, eventually leading to breakup of the drop into two large and one small (satellite) droplets. The symmetry and smoothness of the bulk surfactant concentration contours may be considered as an indication of the accuracy of the computations. The grid convergence of the method is shown in Fig. 14 where the deformation is plotted for 32×96 , 64×192 and 128×384 grid resolutions. The deformation is defined as

$$D_L = \frac{L_d - 2a}{2a}, \quad (52)$$

where L_d is the length of the drop in the axial direction and a is the initial radius of the droplet. The reduction of the differences between the deformations computed on successively finer grids indicates the grid convergence of the method.

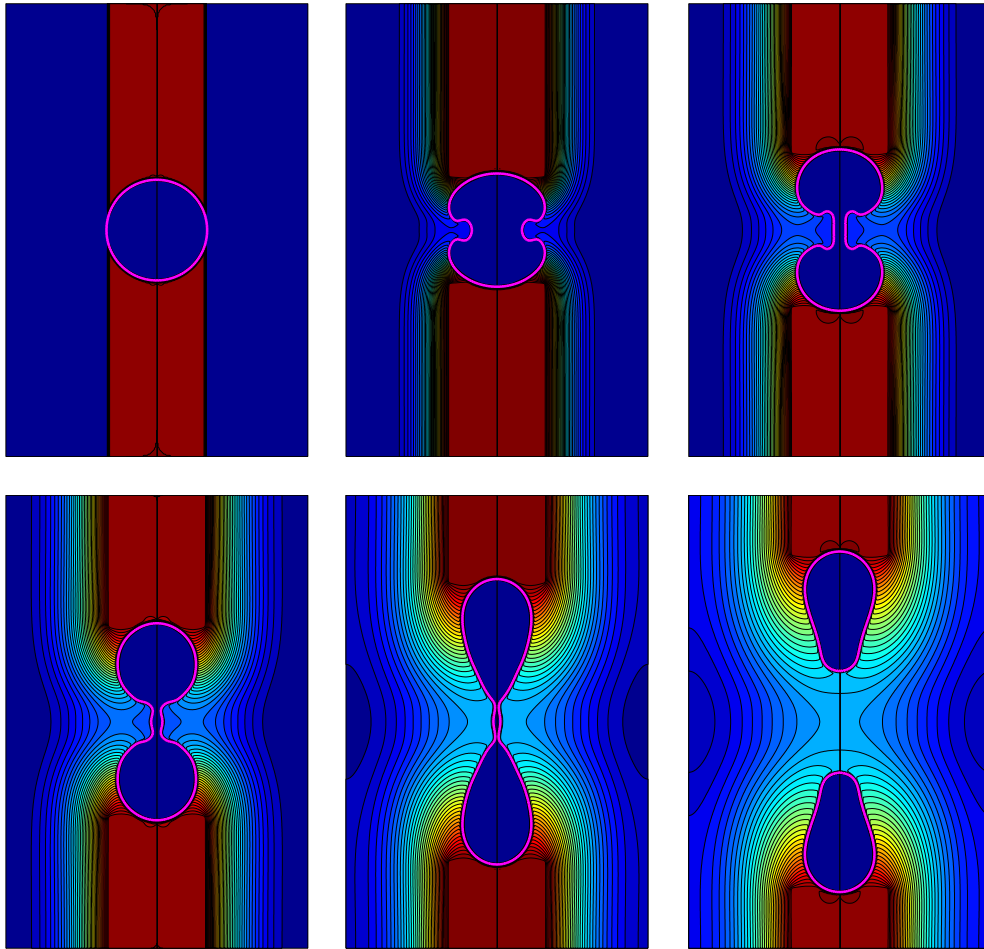


Fig. 11. Cleavage of a viscous drop by surfactant. The drop interface is plotted together with the bulk surfactant concentration contours at times $t^* = 0, 74.9, 150.1, 187.5, 287.5$ and 450 . Time progresses from left to right and top to bottom. The bulk concentration is kept constant at the poles to simulate continuous supply of surfactant. Grid: 128×384 . (For interpretation of the references to colours, the reader is referred to the web version of this paper.)

A detailed analysis of this problem will be reported in a separate paper where effects of the various parameters on the drop cleavage will be studied.

5.2. Buoyancy-driven rising bubbles

We next apply the method to study the effects of soluble surfactants on the motion and deformation of buoyant viscous bubbles rising in an axisymmetric tube. We consider a straight cylindrical capillary tube of radius R and assume that the flow is axisymmetric. The computational domain size is R in radial direction and L in the axial direction. Periodic boundary conditions are applied in the axial direction, i.e., we simulate a chain of bubbles rising in an infinitely long channel and L is the distance between the bubbles. Symmetry and no-slip boundary conditions are used at the centerline and at the wall of the tube, respectively. The bubble is initially located at the centerline of the tube close to the bottom boundary. The interface is initially clean and the surfactant concentration is uniform in the bulk fluid at $C = C_\infty$. The bubble rises in the tube solely due to density difference between the bubble and the ambient fluids. The problem was studied earlier by Jan [17] for the case of insoluble surfactant using a front-tracking method similar to that used in the present work, and following [17], a buoyancy force, $(\rho - \bar{\rho})\mathbf{g}$, is added to the momentum Eq. (1). Here $\bar{\rho}$ is the average density of the whole flow domain and $\bar{\rho}\mathbf{g}$ is a hydrostatic force added to keep the net vertical momentum constant.

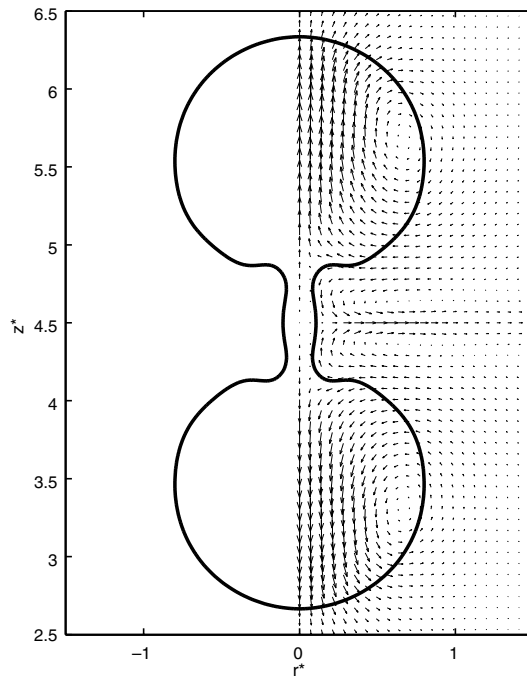


Fig. 12. Velocity vectors shown at every third grid point in the vicinity of the drop just before the drop cleavage. Grid: 128×384 and $t^* = 237.5$.

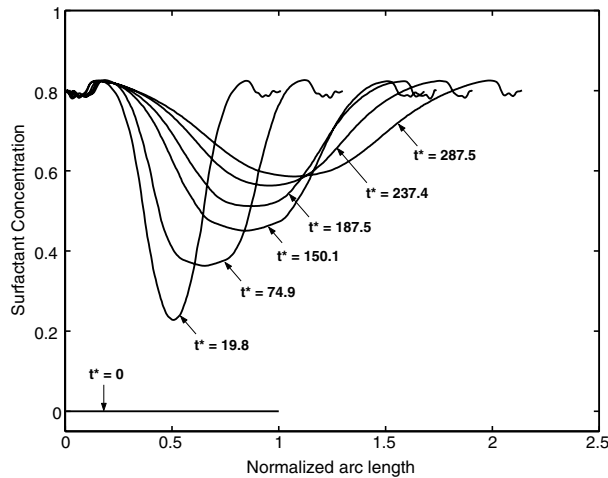


Fig. 13. Cleavage of a viscous drop by surfactant. The surfactant concentration at the interface is plotted against normalized arc length at various non-dimensional times.

In addition to the non-dimensional numbers given by Eq. (17), there are four additional independent parameters for this problem: the Eötvös number $Eo = \Delta\rho g d / \sigma_s$, the Morton number $Mo = \Delta\rho g \mu_o^4 / \rho_o^2 \sigma^3$, the non-dimensional channel diameter D/d and the non-dimensional separation between the bubbles in the bubble chain L/d . The length and velocity scales are taken as $\mathcal{L} = d$ and $U = V_{HR}$, respectively, where V_{HR} is the terminal velocity given by Hadamard–Rybczynski solution [6] for a spherical bubble moving in an infinite domain, i.e.,

$$V_{HR} = \frac{2}{3} \frac{ga^2 \Delta\rho}{\mu_o} \frac{\mu_o + \mu_b}{2\mu_o + 3\mu_b}, \tag{53}$$

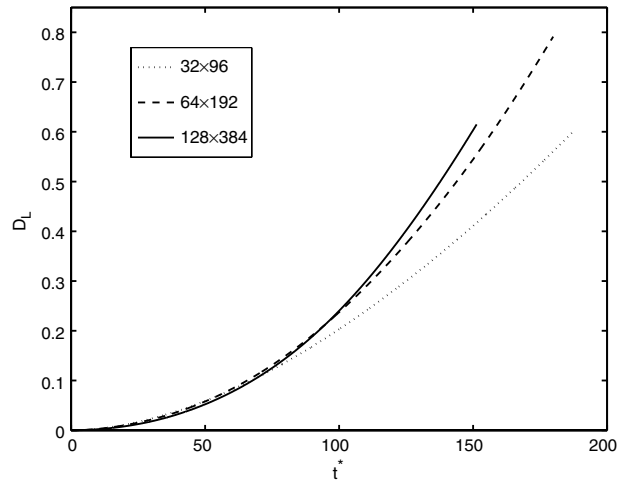


Fig. 14. Deformation versus non-dimensional time using various grid resolutions.

where a is the bubble radius. The time scale is then defined as $T = \mathcal{L}/U$. The parameters Pe_c , P_s , Bi and Da are defined based on these scales. However non-dimensional time (t^*) and Reynolds number (Re) are defined using the actual bubble terminal velocity (V_b) as the velocity scale and $\sqrt{d/g}$ as the time scale in order to facilitate direct comparison of the computational results with available experimental data.

Numerous experimental studies [6] have shown that in the limit of low Reynolds number, i.e., $Re < 1$, contaminated bubble behaves like a solid sphere rather than a fluid sphere so that the terminal velocity of a contaminated bubble approaches that of an equivalent solid sphere. This problem is studied here and the computational results are compared with experimental data both for clean and contaminated bubbles. Here, the non-dimensional parameters are $\frac{\rho_d}{\rho_o} = 0.1$, $\frac{\mu_d}{\mu_o} = 0.025$, $Pe_c = 10$, $P_s = 100$, $k = 1$, $Da = 0.2$, $Bi = 20$ and $\beta_s = 0.5$. The Eötvös and Morton numbers are chosen as $Eo = 1$ and $Mo = 0.1$ for which the theoretical, steady-state Reynolds number of a clean bubble in an unbounded domain is 0.26, which is well within the validity of the theory. Fig. 15 shows a contaminated bubble moving in a channel with $D/d = L/d = 15$ at several times. The computational domain is resolved by a 288×576 uniform grid, i.e., the bubble is resolved by approximately 39 grid points in the axial direction. The surfactant concentration in the bulk fluid is plotted as contour plots on the left side of Fig. 15(a) while the surfactant concentration at the interface is plotted as dashed lines perpendicular to the bubble interface (thick line), with the length of the dashed lines proportional to the concentration (the actual thickness of the contaminant layer is only a few molecular diameter), on the right side of the same figure. The surfactant concentration initially increases everywhere at the interface and decreases in the bulk fluid near the bubble. At the same time, the surfactant at the interface is swept to the back of the bubble by the oncoming fluid, which significantly reduces the surface tension at the back of the bubble. The surface tension gradient results in a tangential interfacial force that opposes the flow. The interface surfactant concentration eventually reaches a nearly steady distribution. After that the bulk concentration is adsorbed mostly at the front of the bubble, swept to the back and then released to the bulk fluid from the back of the bubble, since the concentration exceeds the equilibrium concentration at the back. In fact, this is the mechanism responsible for the tip streaming [6,24]. The velocity vectors and streamlines are plotted in Fig. 15(b) for the same case in a frame moving with the bubble centroid. The velocity vectors are plotted at every other grid point in order to better show the flow field. As can be seen in the figure, a big vortex is created inside the bubble when the bubble is clean and the vortex nearly vanishes when the surfactant concentration at the bubble interface reaches its steady distribution. The streamline patterns also change as the bubble gets contaminated (right-hand side of Fig. 15(b)) and the spacing of streamline is smaller when the bubble is clean and becomes larger as the bubble gets contaminated. Fig. 15(b) also shows that the bubble interface becomes nearly immobile when the bubble reaches its steady motion and a boundary layer is created at the interface. This can be better seen in Fig. 16 where the flow fields for the clean and contaminated

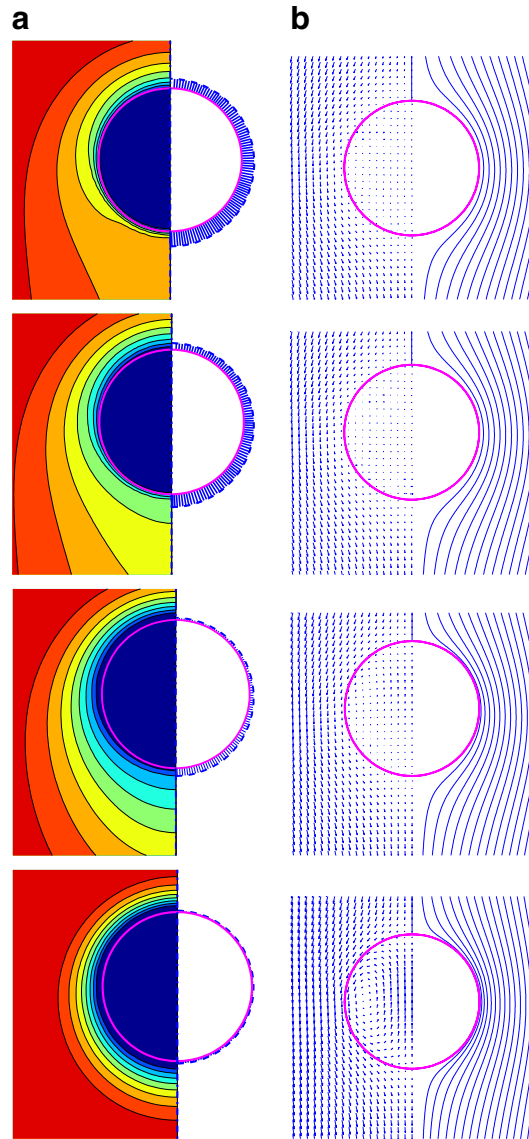


Fig. 15. Snapshots of a contaminated bubble rising in a large axisymmetrical tube at the non-dimensional times (from bottom to top) $t^* = 3.062, 15.309, 56.134$ and 86.753 . (a) The contours of the constant surfactant concentration in the bulk fluid (left) and the distribution of the surfactant concentration at the interface (right). (b) The velocity vectors (left) and the streamlines in the vicinity of the bubble in the frame moving with the bubble centroid. ($Eu = 1, Mo = 0.1, D/d = 15, L/d = 15, \beta_s = 0.5$). (For interpretation of the references to colours, the reader is referred to this web version of this paper.)

bubbles are shown. Again, every other grid point is plotted for clarity. Here, it is clear that there is a large vortex in the clean bubble while the fluid is nearly motionless in the contaminated bubble.

We next examine the grid convergence of the method for the contaminated buoyancy-driven bubble case. For this purpose, we employ an axisymmetric channel with a diameter of $D = 5d$ and a distance between the bubbles equal to $L = 15d$ using various grid resolutions ranging between 32×192 and 128×768 . All other parameters are the same as in Fig. 15. The non-dimensional axial location of the bubble centroid is plotted as a function of time for these grid resolutions in Fig. 17(a). It is clear that a grid convergence is achieved essentially after 64×384 grid resolution. This is quantified in Fig. 17(b) where the axial location of the bubble is plotted at times $t^* = 40, 50$ and 60 as a function of M^{-2} where M is the total number of grid points in the radial direction. A nearly linear relation between z_c^* and M^{-2} indicates a second order spatial accuracy. It can

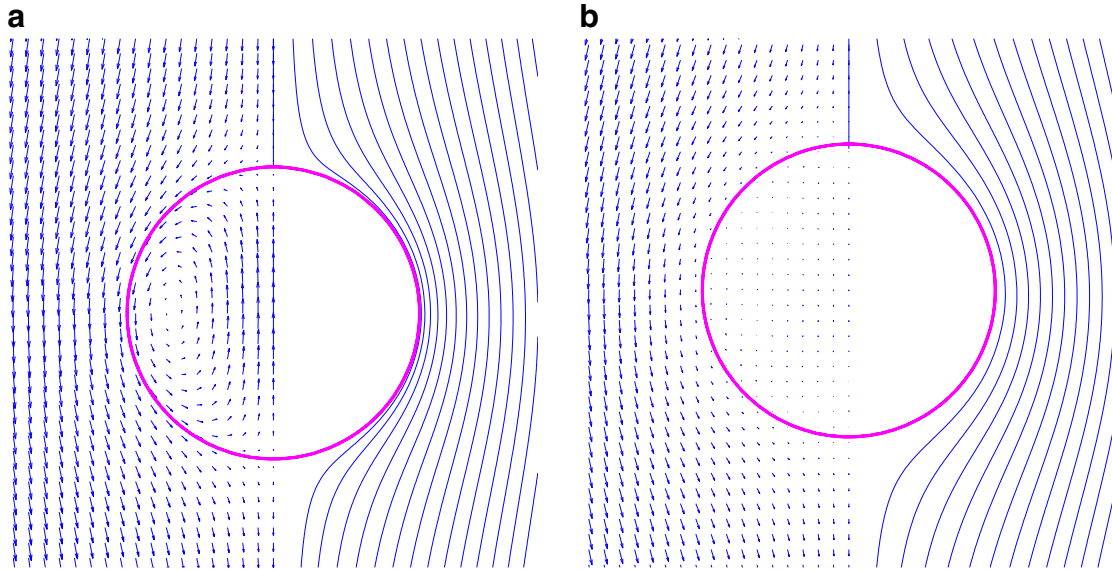


Fig. 16. The streamlines and the velocity vectors in a frame of reference moving with the bubble centroid: (a) clean bubble; (b) contaminated bubble.

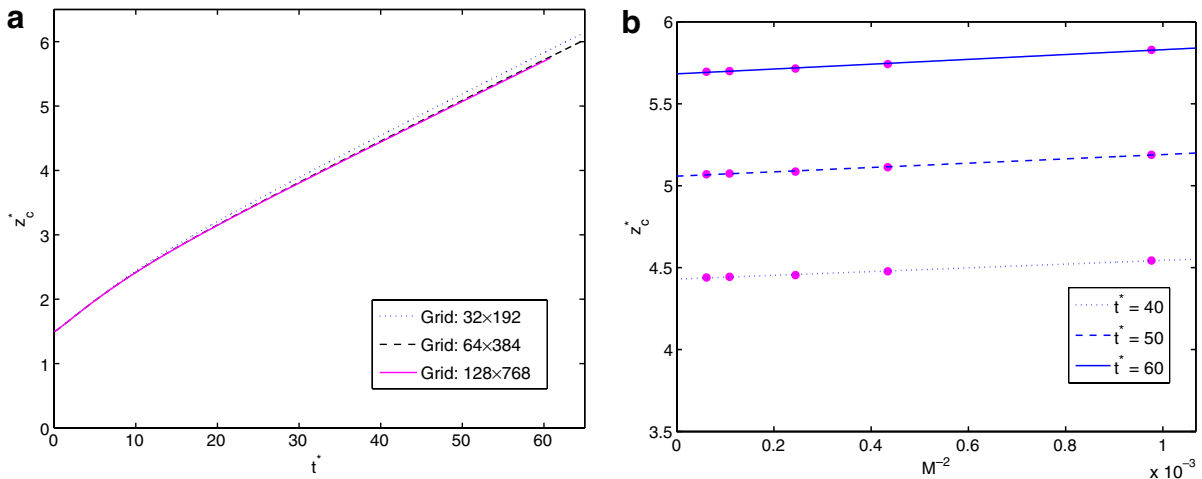


Fig. 17. Grid Convergence test. (a) The non-dimensional axial coordinate of bubble centroid plotted against the non-dimensional time computed on 32×192 , 64×384 and 128×768 grids. (b) The non-dimensional axial coordinate of the bubble centroid against M^{-2} (M is total number of grid points in radial direction) at $t^* = 40, 50$ and 60 .

also be deduced from Fig. 17(b) that the spatial error is overall small and that a 96×576 grid is sufficient to reduces the spatial discretization error below 1% for this case.

We now study the effects of surfactant on the terminal velocity of bubbles moving in an axisymmetrical channel of various diameters. For this purpose, computations are performed for clean and contaminated bubbles moving in a channel with the diameters ranging between $D = 2.5d$ and $D = 15d$. The computations are repeated for two different values of the distance between the bubbles, i.e., $L = 10d$ and $L = 15d$ to show the effects of the interactions between the bubbles on the terminal velocity. All the other parameters are the same as before, i.e., as in Fig. 15. The variation of the Reynolds number is plotted, respectively, in Fig. 18(a) and (b) as a function of non-dimensional time for the clean and contaminated bubbles moving

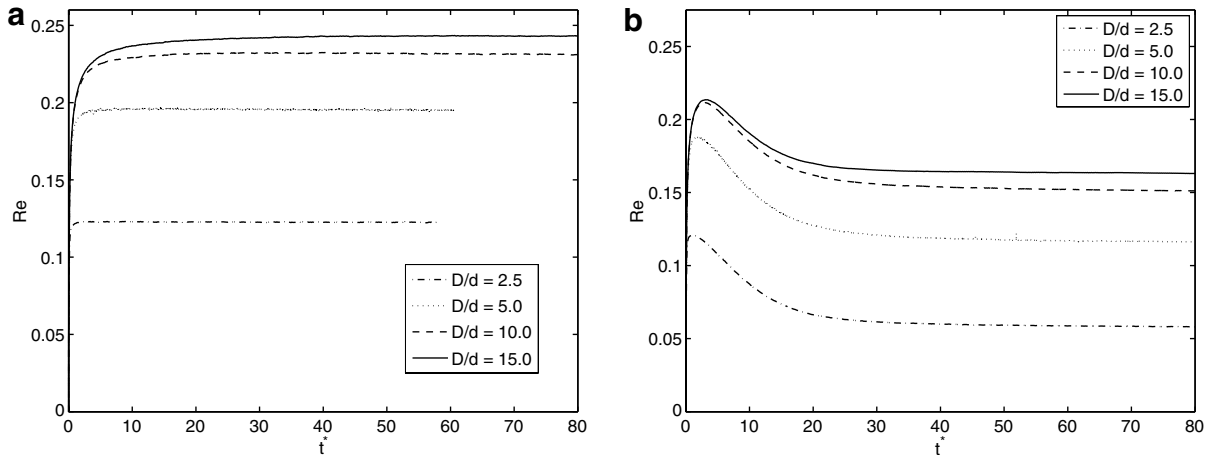


Fig. 18. Reynolds number versus non-dimensional time for the non-dimensional channel diameters $D/d = 2.5, 5.0, 10.0$ and 15.0 for (a) clean and (b) contaminated bubble cases. ($L/d = 15$).

in a channel with $D/d = 2.5, 5.0, 10.0$ and 15.0 , and $L = 15d$. The retardation effect of the surfactant is clearly seen in these figures, i.e., in the clean case, the bubble continuously accelerates and reaches a steady Reynolds number (or terminal velocity) while, in the contaminated case, the bubble first accelerates, reaches a peak velocity but then decelerates as the surfactant accumulates at the interface and finally reaches a steady Reynolds number. The computed steady Reynolds number is plotted in Fig. 19(a) and compared with available experimental data collected by Clift et al. [6] both for the clean and contaminated cases. The computations are performed for two different non-dimensional distances between the bubbles, i.e., $L = 10d$ and $L = 15d$. The computational results are shown by connected symbols while the experimental data are shown by dashed and solid lines for the fluid and solid spheres, respectively. As can be seen in this figure, the computed steady Reynolds number is always larger than the experimental values but the difference between the computed and the experimental Reynolds numbers decreases as the distance between the bubbles gets larger. This is quantified in Fig. 19(b) where the percentage difference between the computed and experimental Reynolds numbers is plotted as a function of the non-dimensional channel diameter for two different values of L/d . It is clearly seen in this figure that the percentage error decreases as either the non-dimensional distance between the

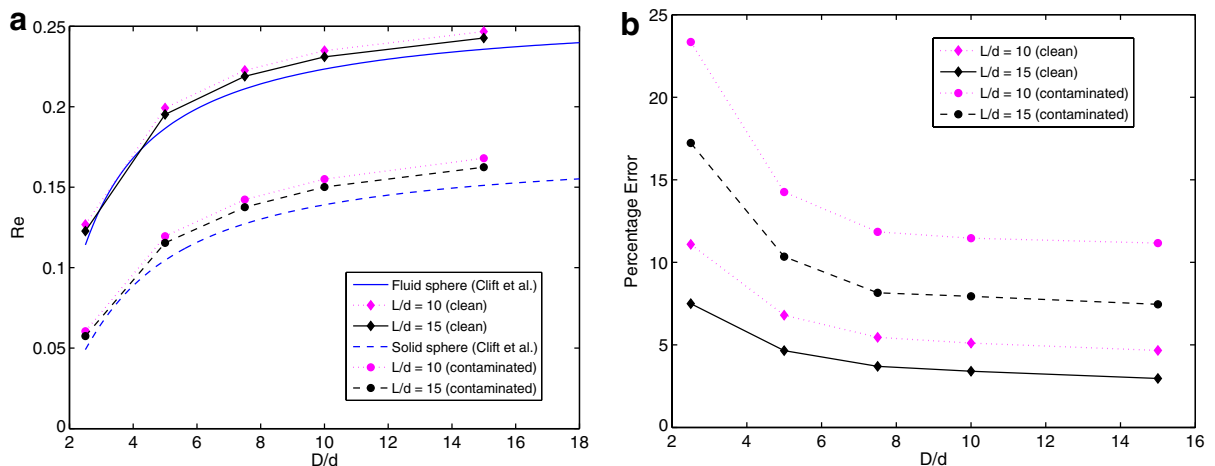


Fig. 19. (a) Reynolds number versus diameter ratio (D/d) for clean and contaminated bubbles. (b) The percentage difference between the computed and experimental steady Reynolds numbers. ($Eu = 1, Mo = 0.1$).

bubbles in the chain or the non-dimensional channel diameter increases. It is also clearly seen from Figs. 19(a) and (b) that the steady Reynolds number of the contaminated bubble approaches that of a solid sphere.

The mass conservation of the surfactant is of crucial importance and may be considered as a good indication of the accuracy of the numerical algorithm. This is quantified by the surfactant mass error defined as

$$\epsilon_{\text{mass}} = \frac{|\Delta M_b + \Delta M_s|}{M_{\text{seq}}}, \tag{54}$$

where M_b and M_s are the total masses of surfactant in the bulk fluid and at the interface, respectively, and M_{seq} is defined as the total mass of surfactant of an equivalent bubble for an equilibrium surfactant distribution at the interface, i.e., $\Gamma_{\text{eq}} = \frac{k}{1+k} \Gamma_{\infty}$. In Eq. (54), ΔM_b and ΔM_s denote the differences between the current and the initial masses in the bulk fluid and at the interface, respectively. The mass error is plotted in Fig. 20 for various non-dimensional channel diameters versus non-dimensional time. The mass error increases at early times, reaches a maximum value and then starts decreasing. In general, the mass error increases faster when the non-dimensional channel diameter gets larger since the bubble moves faster in larger channels. Although the bubble moves up to 10 times its diameter, the maximum mass error is less than 1.8% in all the cases.

Finally the performance of the present method is examined for a strongly deforming contaminated bubble case. For this purpose, the Eötvös and Morton numbers are set to $Eu = 10$ and $Mo = 10^{-3}$, respectively. The channel size is chosen as $D = 5d$ and $L = 30d$, and the other parameters are $\frac{\rho_d}{\rho_o} = 0.1$, $\frac{\mu_d}{\mu_o} = 0.025$, $Pe_c = 100$, $Pe_s = 100$, $k = 1$, $Da = 0.2$, $Bi = 0.75$ and $\beta_s = 0.5$. The computational domain is resolved by a 128×1536 uniform grid. The bubble interface together with contour plots of the surfactant concentration in the bulk fluid (left side) and the surfactant concentration distribution at the interface (right side) are shown in Fig. 21. This figure shows that the surfactant adsorbed by the interface is swept to back of the bubble by the oncoming flow and accumulates there. The steady distribution of the surfactant at the interface results in a force balance between the shear stress caused by the oncoming flow and the tangential Marangoni stresses due to the surface tension gradient. The evolution of the surfactant concentration is plotted in Fig. 22. It is clear that the interfacial surfactant concentration is very small at the front of the bubble and rapidly increases near the normalized arc length of $s^* = 0.6$ and then becomes nearly flat again at the back. This is a typical behavior of a stagnant cap regime [6]. In order to show grid convergence, computations are performed using various grid resolutions ranging between 32×384 and 256×3072 . The surfactant mass error and the terminal Reynolds number are plotted in Figs. 23(a) and 24(a), respectively, as a function of the non-dimensional bubble centroid for these grid resolutions. Note that the vertical dashed lines shown in Figs. 23(a) and 24(a) are drawn to mark the locations where the spatial error is quantified as discussed below. As can be seen in

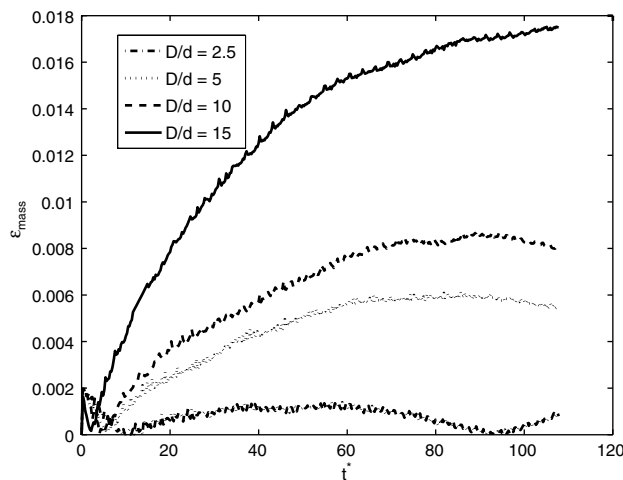


Fig. 20. The surfactant mass conservation error versus the non-dimensional time.

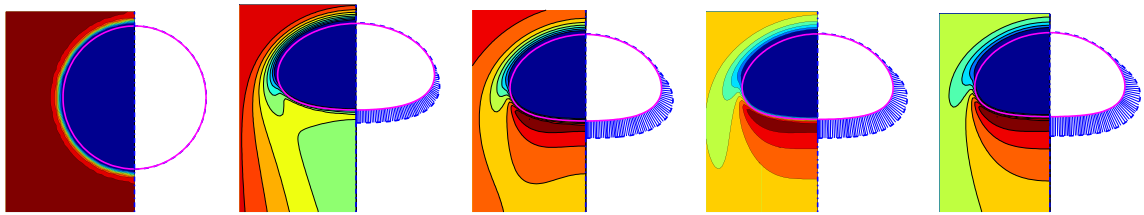


Fig. 21. The contour plots of the constant surfactant concentration in the bulk fluid (left) and the distribution of the surfactant concentration at the interface (right) for a rising contaminated bubble. $Eo = 10$, $Mo = 10^{-3}$ and $\beta_s = 0.5$. Snapshots are taken at the non-dimensional times (from left to right) $t^* = 0.0, 9.68, 19.36, 28.40$ and 38.73 . (Grid: 128×1536). (For interpretation of the references to colours, the reader is referred to the web version of this paper.)

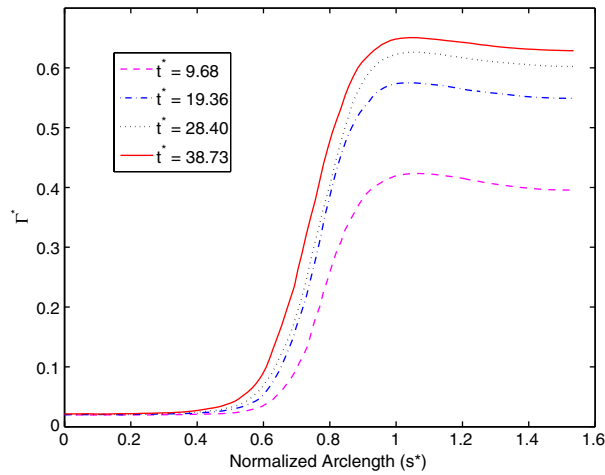


Fig. 22. Variation of interfacial surfactant concentration as a function of non-dimensional arc length measured from the centerline in the clockwise direction at non-dimensional times $t^* = 9.68$ (dashed line), 19.36 (dashed-dotted line), 28.40 (dotted line), and 38.73 (solid line). ($Eo = 10$, $Mo = 10^{-3}$, $\beta_s = 0.5$).

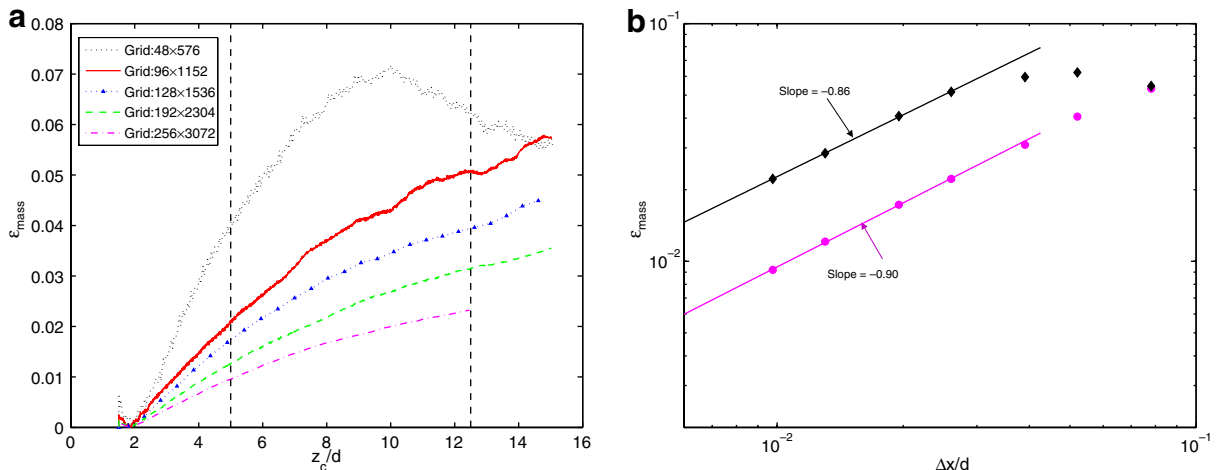


Fig. 23. (a) The variation of surfactant mass error as a function of the non-dimensional axial location of the bubble centroid computed using various grid resolutions ranging between 48×576 and 256×3072 . (b) The surfactant mass error versus the non-dimensional grid size at $z_c/d = 5$ and $z_c/d = 12.5$. ($Eo = 10$, $Mo = 10^{-3}$, $\beta_s = 0.5$).

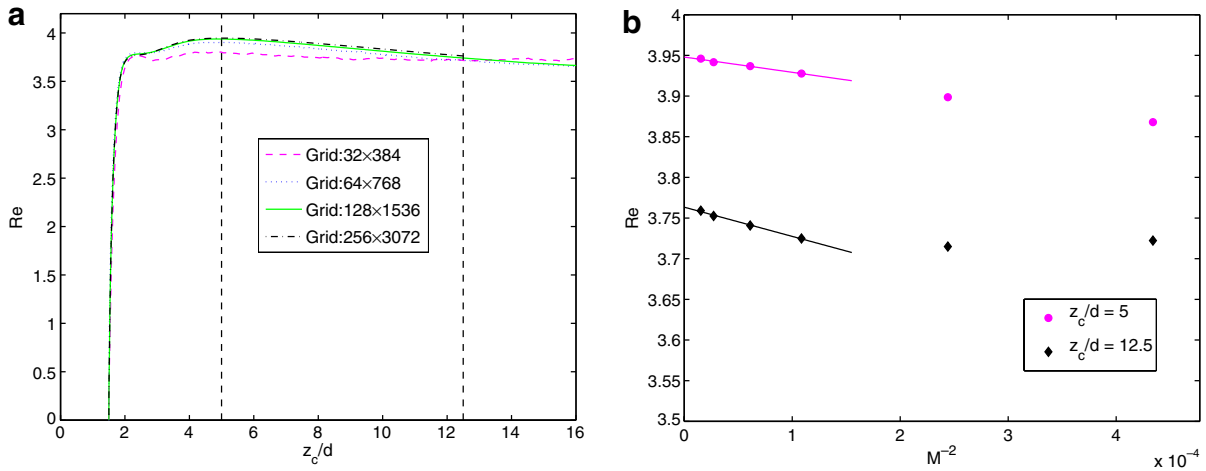


Fig. 24. (a) The variation of Reynolds number as a function of the non-dimensional axial location of the bubble centroid computed using various grid resolutions ranging between 32×384 and 256×3072 . (b) The Reynolds number versus M^{-2} (M is the total number of grid cells in the radial direction) at the axial locations of $z_c/d = 5$ and $z_c/d = 12.5$. ($Eu = 10, Mo = 10^{-3}, \beta_s = 0.5$).

Fig. 23(a), the surfactant mass error decreases towards zero as the grid is refined. The surfactant mass error is quantified in Fig. 23(b) where it is plotted as a function of grid size at two non-dimensional axial locations of the bubble centroid, i.e., at $z_c/d = 5$ and $z_c/d = 12.5$. This figure clearly shows that the 128×1536 grid resolution is sufficient to reduce the surfactant mass error below 5% at both locations and the spatial accuracy is slightly smaller but close to unity. Note that the spatial accuracy reduces to first order near the interface due to the smoothing of discontinuous fields such as the bulk surfactant concentration in the vicinity of the interface. The spatial accuracy of the terminal velocity is also quantified in Fig. 24(b). In this figure, the terminal velocity is plotted as a function of M^{-2} where M is again the number of grid points in the radial direction. It is seen that a 128×1536 grid resolution is sufficient to reduce the spatial error in the terminal Reynolds number below 2% at both locations.

6. Conclusions

A finite-difference/front-tracking method is developed for computations of interfacial flows with soluble surfactants. The method is designed to solve the interface and bulk surfactant concentration evolution equations coupled with the incompressible flow equations. It can employ virtually any non-linear equation of state that relates interfacial tension to the surfactant concentration at the interface. The method is very flexible in the sense that bulk surfactant may be present in the ambient or the drop fluids, or in both fluids with different concentrations. Furthermore, it is straightforward to extend the method to simulate cases where the surfactant is created at the interface as a result of a chemical reaction between the solutes in the drop and bulk fluids.

The method is validated using simple test cases for which analytical solutions are available. It is found that the computational results are in a good agreement with the analytical solutions for all the tests. The method is then applied to the cleavage of a drop by surfactant—a problem proposed as a model for cleavage of biological cells. It is found that strong surfactants introduced at the poles of an axisymmetrical drop may cause the drop to break into two large and one small (satellite) droplets. Finally the method is used to simulate the effects of a soluble surfactant on the motion and deformation of buoyancy-driven viscous bubbles in a straight axisymmetrical channel of various diameters. It is found that the contaminated bubble behaves like a solid sphere in the limit of low Reynolds number, i.e., $Re < 1$ and the computational results are found to be in a good agreement with the experimental correlations collected by Clift et al. [6] both for the clean and contaminated cases. Then the method is successfully used to simulate the motion and deformation of a strongly deforming contaminated bubble in an axisymmetrical channel. It is found that the steady interfacial surfactant concentration distribution is similar to that of a stagnant-cap regime [6] for this case.

The grid convergence of the method has been demonstrated for all the cases studied in the present paper. The mass conservation of the surfactant is quantified and it is found that the surfactant mass conservation error is small, especially for the cases of smooth variation of the bulk surfactant concentration near the interface. The method is overall second order accurate in space but the spatial accuracy reduces to first order for the surfactant mass conservation mainly due to smoothing of the source term at the interface.

Acknowledgments

The computations are performed using the high performance computing center at Koc University. The first author (MM) is supported by the Scientific and Technical Research Council of Turkey (TUBITAK), Grant 105M043.

References

- [1] J.C. Adams, Mudpack: Multigrid Fortran software for the efficient solution of linear elliptical partial differential equations, *Appl. Math. Comput.* 34 (1989) 113.
- [2] S.L. Anna, H.C. Meyer, Microscale tip streaming in a microfluidic flow focusing device, *Phys. Fluids* 18 (12) (2006). Art. No. 12151.
- [3] M.E. Avery, J. Mead, Surface properties in relation to atelectasis and hyaline membrane disease, *Am. J. Dis. Child* 97 (1959) 517.
- [4] A. Borhan, C.F. Mao, Effect of surfactants on the creeping motion of drops through circular tubes, *Phys. Fluids A* 4 (12) (1992) 2628.
- [5] A.R. Chorin, Numerical solution of the Navier–Stokes equations, *Math. Comput.* 22 (1968) 745.
- [6] R. Clift, J.R. Grace, M.E. Weber, *Bubbles, drops and particles*, Dover (2005).
- [7] M.A. Drumright-Clarke, Y. Renardy, The effect of insoluble surfactant at dilute concentration on drop breakup under shear with inertia, *Phys. Fluids* 16 (1) (2004) 14.
- [8] C.D. Eggleton, K.J. Stebe, An adsorption–desorption controlled surfactant on a deforming droplet, *J. Coll. Int. Sci* 208 (1998) 68.
- [9] C.D. Eggleton, T.M. Tsai, K.J. Stebe, Tip-streaming from a drop in the presence of surfactants, *Phys. Rev. Lett.* 87 (2001) 048302.
- [10] M. Faivre, T. Ward, M. Abkarian, A. Vierrat, H.A. Stone, Production of surfactant at the interface of a flowing drop: Interfacial kinetics in a microfluidic device, in: 57th APS Division of Fluid Dynamics Meeting, Seattle, WA, USA, 2004.
- [11] H. Fujioka, J.B. Grotberg, The steady propagation of a surfactant-laden liquid plug in a two-dimensional channel, *Phys. Fluids* 17 (8) (2005) 082102.
- [12] H.P. Greenspan, On the dynamics of cell cleavage, *J. Theor. Biol.* 65 (1) (1977) 79.
- [13] H.P. Greenspan, On fluid-mechanical simulations of cell division and movement, *J. Theor. Biol.* 70 (1) (1978) 125.
- [14] X. He, M. Dembo, On the mechanics of the first cleavage division of the sea urchin egg, *Exp. Cell Res.* 233 (1997) 252.
- [15] Z. He, Z. Dagan, C. Maldarelli, The influence of surfactant adsorption on the motion of a fluid sphere in a tube. Part 1. Uniform retardation controlled by sorption kinetics, *J. Fluid Mech.* 222 (1991) 1.
- [16] A.J. James, J. Lowengrub, A surfactant-conserving volume-of-fluid method for interfacial flows with insoluble surfactants, *J. Comp. Phys.* 201 (2004) 685.
- [17] Y.J. Jan, Computational studies of bubble dynamics, Ph.D. Thesis, The University of Michigan, 1994.
- [18] R.A. Johnson, A. Borhan, Pressure-driven motion of surfactant-laden drops through cylindrical capillaries: effect of surfactant solubility, *J. Colloid Interf. Sci.* 261 (2003) 529.
- [19] J. Lee, C. Pozrikidis, Effects of surfactants on the deformation of drops and bubbles in Navier–Stokes flow, *Comput. Fluids* 35 (1) (2006) 43.
- [20] V.G. Levich, *Physicochemical Hydrodynamics*, Prentice Hall, 1962.
- [21] W.J. Milleken, H.A. Stone, L.G. Leal, The effect of surfactant on transient motion of newtonian drops, *Phys. Fluids A* 5 (1993) 69.
- [22] C. Peskin, Numerical analysis of blood flow in the heart, *J. Comput. Phys.* 25 (1977) 220.
- [23] H.A. Stone, A.D. Stroock, A. Ajdari, Engineering flows in small devices: Microfluidics toward lab-on-a-chip, *Annu. Rev. Fluid Mech.* 36 (2004) 381.
- [24] H.A. Stone, Dynamics of drop deformation and breakup in viscous fluids, *Annu. Rev. Fluid Mech.* 26 (1994) 65.
- [25] H.A. Stone, A simple derivation of the time-dependent convective–diffusion equation for surfactant transport along a deforming interface, *Phys. Fluids A* 2 (1990) 111.
- [26] H.A. Stone, L.G. Leal, The effects of surfactants on drop deformation and breakup, *J. Fluid Mech.* 220 (1989) 161.
- [27] G. Tryggvason, B. Bunner, A. Esmaeili, D. Juric, N. Al-Rawahi, W. Tauber, J. Han, S. Nas, Y.-J. Jan, A front-tracking method for the computations of multiphase flow, *J. Comput. Phys.* 169 (2) (2001) 708.
- [28] T.M. Tsai, M.J. Miksis, The effects of surfactant on the dynamics of bubble snap-off, *J. Fluid Mech.* 337 (1997) 381.
- [29] S.O. Unverdi, G. Tryggvason, A front-tracking method for viscous incompressible multiphase flows, *J. Comput. Phys.* 100 (1992) 25.
- [30] E.A. van Nierop, A. Ajdari, H.A. Stone, Reactive spreading and recoil of oil on water, *Phys. Fluids* 18 (3) (2006). Art. No. 03810.
- [31] J.-J. Xu, Z. Li, J. Lowengrub, H. Zhao, A level-set method for interfacial flows with surfactant, *J. Comput. Phys.* 212 (2006) 590.
- [32] N.O. Young, J.S. Goldstein, M.J. Block, The motion of bubbles in a vertical temperature gradient, *J. Fluid Mech.* 6 (1959) 350.
- [33] J. Zhang, D.M. Eckmann, P.S. Ayyaswamy, A front tracking method for a deformable intravascular bubble in a tube with soluble surfactant transport, *J. Comput. Phys.* 214 (1) (2006) 366.